On the Lateral Instability Analysis of MEMS Comb-Drive Electrostatic Transducers

Binh Duc Truong * , **Cuong Phu Le and Einar Halvorsen**

Faculty of Technology, Natural Sciences and Maritime Sciences, University of South-Eastern Norway, Campus Vestfold, Raveien 215, 3184 Borre, Norway
* Correspondence: Binh.Truong@usn.no

check for updates

Abstract: This paper investigates the lateral pull-in effect of an in-plane overlap-varying transducer. The instability is induced by the translational and rotational displacements. Based on the principle of virtual work, the equilibrium conditions of force and moment in lateral directions are derived. The analytical solutions of the critical voltage, at which the pull-in phenomenon occurs, are developed when considering only the translational stiffness or only the rotational stiffness of the mechanical spring. The critical voltage in a general case is numerically determined by using nonlinear optimization techniques, taking into account the combined effect of translation and rotation. The influences of possible translational offsets and angular deviations to the critical voltage are modeled and numerically analyzed. The investigation is then expanded for the first time to anti-phase operation mode and Bennet's doubler configuration of the two transducers.

Keywords: lateral instability; MEMS electrostatic transducer; static pull-in

1. Introduction

The comb-drive electrostatic transduction is one of the most popular mechanisms used in Microelectromechanical systems (MEMS) due to its many inherent advantages such as high efficiency and low power consumption. Various comb-drive electrostatic transducers have been early developed and utilized in a wide variety of application, including micro energy harvesting [1,2], microresonators [3,4] and microactuators [5,6]. During operation, a voltage is applied to the device, generating an electrostatic force between fixed and movable electrodes, both in stroke direction and its perpendicular direction. In a critical condition, when the electrostatic force exceeds the mechanical restoring force, a small disturbance could lead to collapsing of the movable fingers to the fixed ones. This restriction is more critical when the MEMS transducer is electrically configured as Bennet's doubler or voltage multiplier [7,8]. Design of comb-drive devices, therefore, requires a comprehensive analysis of a pull-in effect since the travel range and device performance are severely limited by the inherent instability.

The pioneering investigation of pull-in phenomenon was presented in the late 1960s by Nathanson et al. [9], in which the electrostatic deflection of a parallel-plate actuator is modeled by use of a mass-spring system. The maximum possible deflection is derived as one-third of the initial gap. Since then, the nature of pull-in instability has attracted more and more attention. Other than that, instead of focusing on analysis, several researchers turned their interest towards designing of mechanical spring structures to enlarge the maximum displacement, or devising an external control scheme to ensure the device stabilization.

Legtenberg et al. presented an expression for the translational instability voltage and deflection [10]. The theoretical stiffness of various spring structures such as clamped-clamped, crab-led, and folded-beam designs was determined. A similar issue with a tiled folded-beam suspension was investigated by

Zhou et al. [11]. Both theoretical and experimental results show an enhancement of the stable travel range. In these works, the rotational displacement has not been concerned yet.

Pull-in effects due to translational and rotational misalignments are individually analyzed by Avdeev et al. utilizing three approaches: analytical, uncoupled 2D/3D finite element (FE) models and coupled FE model [12]. A good agreement between analytical solutions and coupled FE simulation results show that fringing fields have little effect on the translational pull-in voltage for the comb-drive geometry. The critical voltage (i.e., beyond which the lateral instability occurs) considering both the translational stiffness and the rotational stiffness has not been explored yet.

Huang et al. presented a development of this analysis, taking into account the case when effects of the translational and rotational deflections are comparable [13]. Simplified analytical solutions of the pull-in voltage are obtained based on a two-dimensional model of a single movable comb finger. A simple example with a two-port actuator was analyzed, in which the mechanical stiffnesses were calculated using ANSYS, and the critical voltage was explicitly determined. However, the cross stiffness between the translation and the rotation is neglected.

With the same manner, in this work, we further develop a comprehensive theoretical model to investigate the lateral side instability phenomena for both two-port and three-port transducers. Analytic and numerical results can be adapted to any mechanical spring structure. An analysis that takes into account the effect of a translational or rotational offset due to potential process errors is presented. The general case when the cross stiffness between the two degrees of lateral freedom is included, and the critical voltage for different transducer configurations are numerically studied. Nonlinear optimization techniques with unequal constraints are used due to the complexity of the problem, especially when the two transducers are electrically configured as a Bennet's doubler. A complete design is given as an example without compromising the generality of our study.

2. Analytical Model of a Single Transducer with Translational and Rotational Misalignments

2.1. Device Modeling

Figure 1 shows key features of the overlap-varying electrostatic transducers and addresses potential issues of the general lateral instability. The three-degree-of-freedom (x, y, θ) device includes two ordinary comb-drive structures with proof mass suspended by four linear springs. The rigid end-stops are used to confine the maximum displacement. In an ideal case, the movable fingers are in the center of the gap along the x axis, i.e., the stroke direction, and are in parallel with the fixed ones. The comb-drive fingers are assumed to be rigid since their stiffness is typically designed to be much higher than the spring stiffnesses.

We are now considering the simplest case when a single electrostatic transducer is used as an actuator. Several prototypes were fabricated and evaluated, for instance, see among others [11,14–16]. An example of a circuit diagram for this device type is drawn in Figure 2. As both the translational and rotational displacements are taken into account, i.e., y and θ in the close-up view of Figure 1, capacitances of the transducer can be expressed

$$C_A(x,y,\theta) = C_1(x,y,\theta) + C_2(x,y,\theta) + C_P, \tag{1}$$

where

$$C_1(x,y,\theta) = N\epsilon\epsilon_0 t \int_0^{x_0+x} \frac{1}{g_0 + y + (L-l)\sin\theta} \mathrm{d}l, \tag{2}$$

$$C_2(x,y,\theta) = N\epsilon\epsilon_0 t \int_0^{x_0+x} \frac{1}{g_0 - y - (L-l)\sin\theta} \mathrm{d}l, \tag{3}$$

C_P—the parasitic capacitance, N—a number of the movable fingers, ϵ_0—the permittivity of free space, ϵ—the relative permittivity of the dielectric material, t—the device thickness, x_0—the initial

overlap, x—the proof mass displacement, g_0—the initial gap between fingers, L and dl—the length and a differential segment of the movable finger respectively. As the length of the finger and the thickness of the device (i.e., the electrode dimensions) are much larger than the gap between two fingers, the fringing effect can be ignored. The capacitance created by the finger tips is negligible since the finger thickness is usually much smaller than its length. These equations yield to

$$C_1(x,y,\theta) = C_0 \frac{g_0}{2x_0 \sin\theta} \ln \frac{g_0 + y + L\sin\theta}{g_0 + y + (L - (x_0 + x))\sin\theta}, \tag{4}$$

$$C_2(x,y,\theta) = C_0 \frac{g_0}{2x_0 \sin\theta} \ln \frac{g_0 - y - (L - (x_0 + x))\sin\theta}{g_0 - y - L\sin\theta}, \tag{5}$$

where $C_0 = 2N\epsilon\epsilon_0 t x_0 / g_0$ is the nominal capacitance. Since the maximum displacement $X_{\max}$ is chosen to be smaller or equal to the initial overlap, we get $x_0 \pm x \geq 0$, $\forall x \in [-X_{\max}, X_{\max}]$.
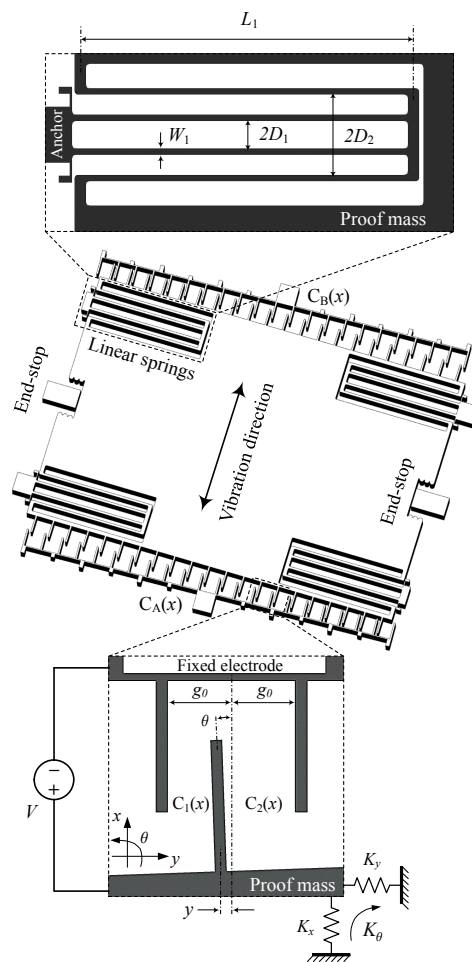

Figure 1. Key features of MEMS electrostatic transducers.
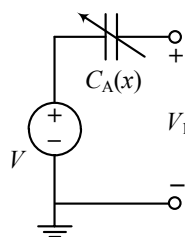

Figure 2. Circuit diagram for a single variable capacitance device.

In this paper, we chose to investigate the folded-beam flexure, as shown in Figure 1, which is one of the most commonly used suspensions in comb-drive transducers/actuators. Adapting from a work presented by Olfatnia et al. [16] which included theoretical analysis and its experimental verification, the stiffness of a single spring are given

$$k_x = \frac{EtW_1^3}{L_1^3}, \tag{6}$$

$$k_y = \frac{EtW_1^3}{L_1} \frac{140}{140W_1^2 + 51x^2}, \tag{7}$$

$$k_\theta = \frac{EtW_1}{L_1} \frac{350W_1^2}{700W_1^2 + 3x^2} \frac{4D_1^2 D_2^2}{D_1^2 + D_2^2}, \tag{8}$$

where E is Young's modulus. The spring length L_1, the spring width W_1, and the beam distances D_1 and D_2 are defined as Figure 1.

The total mechanical spring stiffnesses are $K_x = 4k_x$, $K_y = 4k_y$ and $K_\theta = 4k_\theta$. It is important to observe that the translational and rotational stiffnesses k_y and k_θ respectively decrease with the increase of the displacement x. In addition, k_θ can be made large with respect to the dimensions D_1 and D_2. Figure 3 shows analytical results of K_y and K_θ in comparison with K_x. The drop in K_y and K_θ from its nominal value (at $x = 0$) with increasing x is far more gradual. The detail parameters are summarized in Table 1.
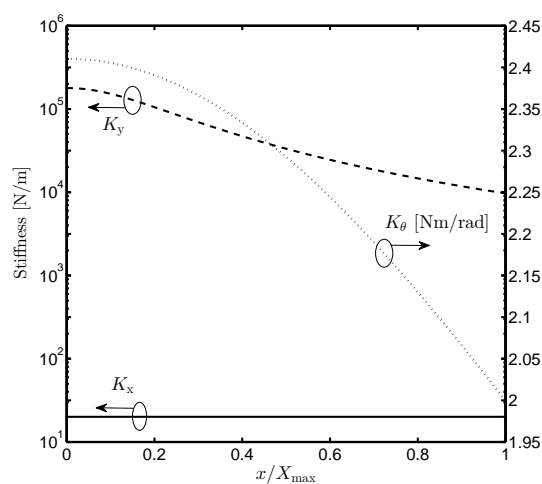

Figure 3. The displacement-dependent spring stiffnesses of the folded-beam flexure design. K_x and K_y: lateral stiffness, K_θ: rotational stiffness.

Table 1. Device structure parameters.

Parameters	Value
Nominal capacitance, C_0	12.27 pF
Device thickness, t	25 μm
Finger length, L	222 μm
Initial gap, g_0	2 μm
Nominal overlap, x_0	110 μm
Spring length, L_1	1500 μm
Spring width, W_1	16 μm
Beam distance, D_1 (D_2)	200 (90) μm
Maximum displacement, X_{max}	110 μm
Young's modulus, E	169 GPa

2.2. Potential Energy

For the sake of simplicity, we only analyze the case $|x| \leq X_{\max}$; the elastic energy of the end-stops is therefore neglected. The total potential energy of the system can be written

$$W = W_{\mathrm{m}} + W_{\mathrm{e}}, \tag{9}$$

where W_{m} is the elastic energy of the springs, W_{e} is the electrostatic energy of the transducers and V is the voltage applied to the electrodes. With the proof mass displaced by x from the equilibrium position, their expressions are

$$W_{\mathrm{m}} = \frac{1}{2} K_x x^2 + \frac{1}{2} K_y y^2 + \frac{1}{2} K_\theta \theta^2, \tag{10}$$

$$W_{\mathrm{e}} = -\frac{1}{2} \left(C_1 + C_2 + C_{\mathrm{p}} \right) V^2. \tag{11}$$

According to the principle of virtual work, the forces and moment associated with the three coordinates x, y and θ can be calculated by

$$F_{\mathrm{x}} = -\frac{\partial W}{\partial x} = -K_x x + \frac{1}{2} V^2 \frac{\partial \left(C_1 + C_2 \right)}{\partial x}, \tag{12}$$

$$F_{\mathrm{y}} = -\frac{\partial W}{\partial y} = -K_y y + \frac{1}{2} V^2 \frac{\partial \left(C_1 + C_2 \right)}{\partial y}, \tag{13}$$

$$M_\theta = -\frac{\partial W}{\partial \theta} = -K_\theta \theta + \frac{1}{2} V^2 \frac{\partial \left(C_1 + C_2 \right)}{\partial \theta}. \tag{14}$$

These forces and moment above characterize the equilibrium condition between the electrostatic forces and the restoring forces produced by the mechanical springs. The transducers are in the state of a static electromechanical equilibrium once all of them are equal to zero. For a constant voltage, the transducers always seek out the orientation with the lowest potential energy. If the equilibrium state corresponds to a local minimum of the potential W, then it is locally stable. A local maximum or a saddle in potential energy corresponds to an equilibrium that is unstable.

Figure 4 shows the total potential energy of the transducers at $x = X_{\max}$ and effect of the lateral translational and rotational displacement on the instability. For instance, considering W as a function of y only, i.e., Figure 4a, in the case of $V = 30$ V and $\theta = 0$, the equilibrium state $y = 0$ is stable as it is a local minimum of W. If $\theta = \theta_{\max}/4$, the equilibrium becomes unstable with the same voltage V and any small perturbation of y leads to the pull-in effect. In Figure 4b, the same phenomenon happens with $V = 100$ V and $y = g_0/4$ as W is a function of θ alone. Figure 4c provides us a more general evaluation of W when different values of the constant voltage are applied. There is one stable equilibrium with $V = 10$ V while those that of $V = 45$ V are unstable. The transducer can exhibit equilibria that are unstable along the y- or θ-direction only or along both the y- and θ-directions. In the following sections, the analytical solution of the critical voltage when considering the rotational or translational instability is developed. The numerical solution taking into account the combined effect of rotation and translation is investigated.
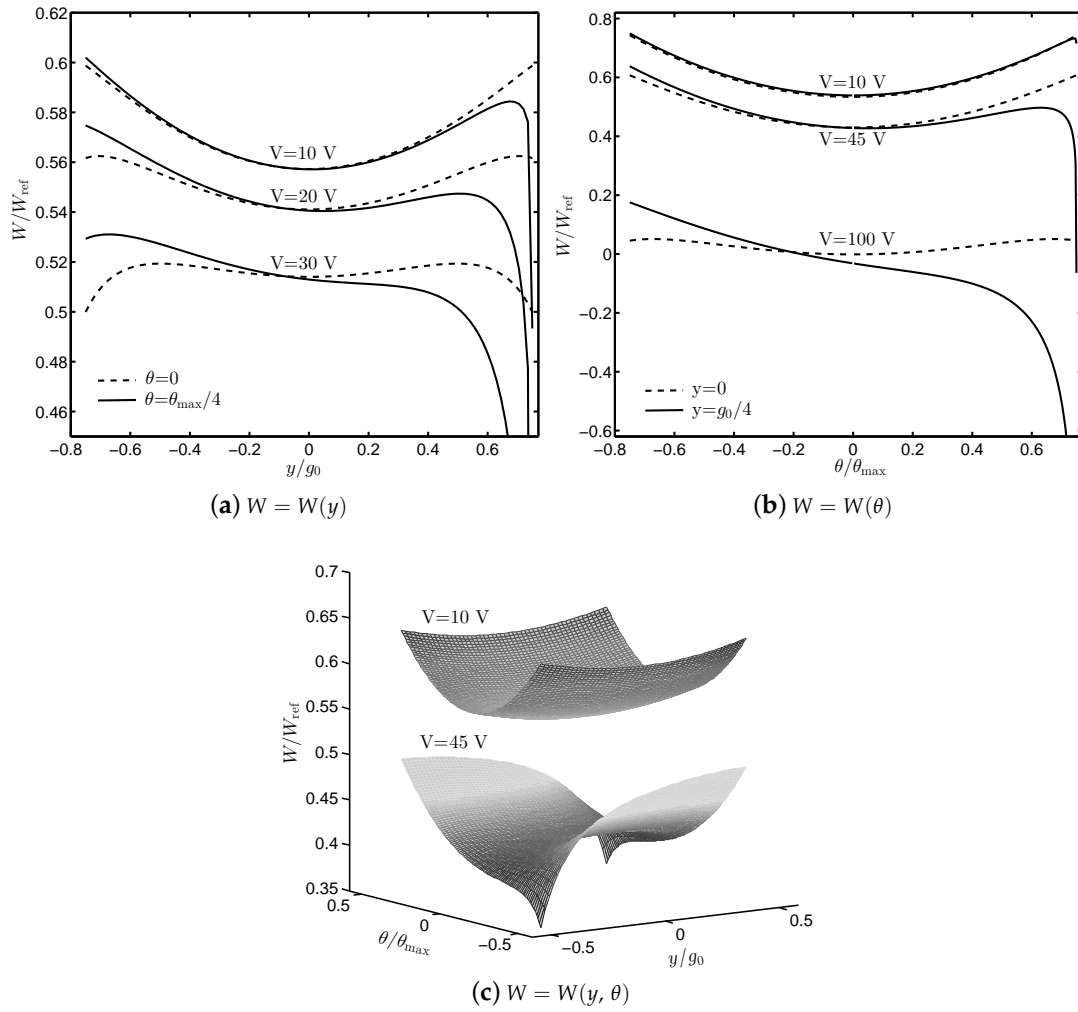
(**a**) $W = W(y)$

(**b**) $W = W(\theta)$

(**c**) $W = W(y, \theta)$

Figure 4. Total potential energy of the transducers as a function of (**a**) the translational displacement y; (**b**) the rotational displacement θ; and (**c**) both y and θ, where $\theta_{\max} = \tan^{-1}(g_0/L)$, $x = X_{\max}$ and $W_{\mathrm{ref}} = K_x x^2/2$.

2.3. Rotational Instability

Assume that the translational stiffness K_y is extremely large and the translation y is negligible. Since θ is small, $\sin\theta \approx \theta$, and the total capacitance is

$$C_{\mathrm{A}} = \frac{1}{2}\frac{C_0 g_0}{x_0 \theta} \ln \frac{(g_0 + L\theta)(g_0 - (L - (x_0 + x))\theta)}{(g_0 - L\theta)(g_0 + (L - (x_0 + x))\theta)} + C_{\mathrm{p}}. \tag{15}$$

The capacitance changes with the stroke direction displacement x and rotational angle θ. When the moving fingers are parallel to the fixed ones (i.e., $\theta = 0$), the capacitance simplifies to the well-known parallel-plate calculation as expected $\lim\limits_{\theta \to 0} C_{\mathrm{A}} = C_0 \left(1 + \dfrac{x}{x_0}\right) + C_{\mathrm{p}}$. However, as will be shown later, this does not indicate that the rotation effect can be neglected.

At equilibrium, the electrostatic moment is balanced by that of the mechanical spring, which implies

$$\frac{\partial^2 W}{\partial \theta^2} = -\frac{\partial M_\theta}{\partial \theta}\bigg|_{\theta \to 0} = K_\theta - \frac{1}{3}V^2 \frac{C_0}{x_0} \frac{(x_0 + x)\left(3L^2 - 3L(x_0 + x) + (x_0 + x)^2\right)}{g_0^2} = 0. \tag{16}$$

The requirement for stability is that the potential energy is concave up, or equivalently $\frac{\partial^2 W}{\partial \theta^2} > 0$. The maximum voltage across the transducer, so-called critical (or pull-in) voltage, to avoid lateral instability due to rotation is given as

$$V_\theta - cr = \sqrt{3\frac{g_0^2 x_0}{C_0} \frac{K_\theta}{(x_0 + x)\left(3L^2 - 3L(x_0 + x) + (x_0 + x)^2\right)}}. \tag{17}$$

If the voltage is greater than $V_{\theta-cr}$, the transducer cannot be in equilibrium, and, within a certain amount of time, the moving electrode will snap against the fixed one.

In case of $x = X_{\max} \approx x_0 \approx \frac{L}{2}$, Equation (17) yields

$$V_{\theta-cr}\Big|_{x=X_{\max}} = \sqrt{\frac{3}{2}\frac{g_0^2}{C_0}\frac{K_\theta}{L^2}}. \tag{18}$$

It is obvious that the increase of the nominal gap g_0 enhances the lateral stability. However, on the other hand, some device functions (e.g., energy harvesters) may require large nominal capacitance $C_0 = 2N\epsilon\epsilon_0 t x_0/g_0$. This requirement could perhaps lead to a decrease of g_0 especially when the initial overlap x_0 is limited. Thus, the design of a mechanical suspension with large K_θ would seem to be the more common point of view to increase the side stability.

As seen in Equation (1), the transducer capacitance is modeled by the ideal-capacitance plus the constant, parallel parasitic capacitance C_p. Under voltage control, the derivatives of the capacitance are functions of displacements, i.e., do not contain C_p anymore. The pull-in voltage is, therefore, independent of C_p. The relationship between charge and displacement in equilibrium (which depends on C_p) is out of the scope in this paper. In the following sections, C_p will be eliminated.

2.4. Translational Instability

As the rotational stiffness is large enough, the rotation can be neglected. Evaluating $\lim_{\theta \to 0}(C_1 + C_2)$ yields

$$C_A = \frac{C_0 g_0^2 (x_0 + x)}{x_0} \frac{1}{g_0^2 - y^2}. \tag{19}$$

The static equilibrium condition is satisfied when

$$\frac{\partial^2 W}{\partial y^2} = \frac{\partial F_y}{\partial y}\Big|_{\substack{\theta \to 0 \\ y \to 0}} = -K_y + V^2 \frac{C_0(x_0 + x)}{x_0 g_0^2} = 0, \tag{20}$$

from which the displacement-dependent critical voltage can be extracted

$$V_{y-cr} = \sqrt{\frac{x_0 g_0^2}{C_0(x_0 + x)} K_y} = \sqrt{\frac{g_0^3}{2N\epsilon\epsilon_0 t(x_0 + x)} K_y}. \tag{21}$$

Based on particular applications of the transducer, one should reasonably expect to make a trade-off between the nominal capacitance C_0 and the initial overlap x_0. For an example, in the case of maximizing the travel range while V_{y-cr} is kept the same, a design of the comb-drive device should have $x_0 = 0$ (or very small), however, yielding to $C_0 = 0$.

Similarly, at the maximum displacement, Equation (21) is simplified as

$$V_{y-cr}\Big|_{x=X_{\max}} = \sqrt{\frac{1}{2}\frac{g_0^2}{C_0} K_y}. \tag{22}$$

Equations (18) and (22) show that the ratio of these two critical voltages is proportional to the root square of the corresponding stiffnesses

$$V_{\text{r−cr}} = \frac{V_{\theta-cr}}{V_{\text{y−cr}}} \propto \sqrt{\frac{K_\theta}{K_y}} \propto \sqrt{\frac{4D_1^2 D_2^2}{D_1^2 + D_2^2}}. \tag{23}$$

The value of $V_{\text{r−cr}}$ can be displacement—independently made large by appropriate choices of the dimensions D_1 and D_2. Figure 5 depicts the variation of $V_{\text{r−cr}}$ with respect to x, in which $V_{\text{r−cr}}$ increases along with the increases of the ratio $\frac{D_1}{D_2}$. Effect of the lateral rotation on the device instability is therefore markedly diminished if $\frac{D_1}{D_2}$ is large enough. For instance, $V_{\theta-cr}$ is about 3.8 times higher than $V_{\text{y−cr}}$ if $D_1 = \frac{1}{2}D_2$. In this case, the lateral translation is more critical.
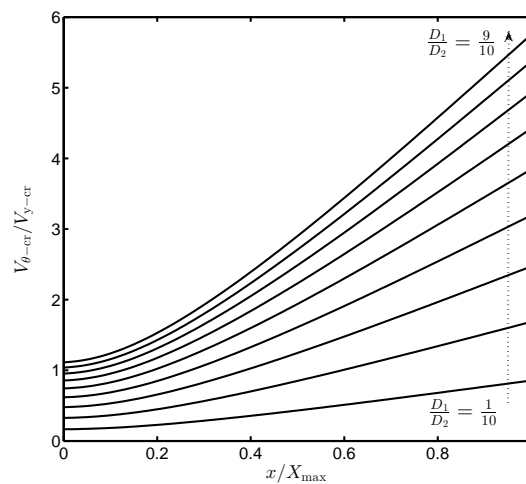

Figure 5. The ratio of rotational and translational critical voltages versus proof mass displacement with different values of $\frac{D_1}{D_2}$.

2.5. Lateral Instability Due to a Combination of Translation and Rotation

In general, when both the translational and rotational displacement are comparable, a stiffness matrix corresponding to the coordinates y and θ contains a cross-interaction terms, i.e., $K_{y\theta}$ and $K_{\theta y}$. Thus far, however, all analyses of the lateral instability of the in-plane comb-drive MEMS transducers have been limited to the neglect of the cross stiffness terms. In this paper, a further developed model taking into account the effect of $K_{y\theta}$ and $K_{\theta y}$ is explored. The moment and force equilibrium conditions now are

$$\begin{bmatrix} F \\ M \end{bmatrix} = \begin{bmatrix} \left.\frac{\partial F_y}{\partial y}\right|_{y\to 0} & \left.\frac{\partial F_y}{\partial \theta}\right|_{\theta\to 0} \\ \left.\frac{\partial M_\theta}{\partial y}\right|_{y\to 0} & \left.\frac{\partial M_\theta}{\partial \theta}\right|_{\theta\to 0} \end{bmatrix} \begin{bmatrix} y \\ \theta \end{bmatrix} = \begin{bmatrix} 0 \\ 0 \end{bmatrix}, \tag{24}$$

where the stiffness coefficients are given by

$$\left.\frac{\partial F_y}{\partial y}\right|_{y\to 0} = -K_y + \frac{1}{4}V^2 \frac{C_0 g_0}{x_0} \left[\frac{4 g_0 L}{(g_0 + L\theta)^2 (g_0 - L\theta)^2} \right.$$
$$\left. + \frac{1}{\theta (g_0 + (L - (x_0 + x))\theta)^2} - \frac{1}{\theta (g_0 - (L - (x_0 + x))\theta)^2} \right], \tag{25}$$

$$\left.\frac{\partial F_y}{\partial \theta}\right|_{\theta\to 0} = \frac{1}{2}V^2 \frac{C_0 g_0^2}{x_0} \frac{(g_0^2 + 3y^2)(x_0 + x)(2L - (x_0 + x))}{(g_0 - y)^3 (g_0 + y)^3}, \tag{26}$$

$$\frac{\partial M_\theta}{\partial y}\Big|_{y\to 0} = \frac{1}{2}V^2\frac{C_0 g_0^2(x_0+x)}{x_0}\left[\frac{\begin{array}{c}g_0^4\left(2L-(x_0+x)\right)-3L^2\theta^4\left(2L-(x_0+x)\right)\left(L-(x_0+x)\right)^2\\ +g_0^2\theta^2\left(4L^3-6L^2(x_0+x)+4L(x_0+x)^2-(x_0+x)^3\right)\end{array}}{\left(g_0-L\theta\right)^2\left(g_0+L\theta\right)^2}\right], \quad (27)$$

$$\frac{\partial M_\theta}{\partial\theta}\Big|_{\theta\to 0} = -K_\theta + \frac{1}{3}V^2\frac{C_0 g_0^2}{x_0}\frac{\left(g_0^2+3y^2\right)\left(x_0+x\right)\left(3L^2-3L(x_0+x)+(x_0+x)^2\right)}{\left(g_0-y\right)^3\left(g_0+y\right)^3}. \quad (28)$$

Let $\overline{V}$ be a set of the parameter V such that Equation (24) has solutions $y \in D_y$ and $\theta \in D_\theta$, and the critical voltage at specific proof mass position is expressed as

$$V_{y,\theta-cr} = \max\left\{V \in \overline{V}\right\}, \quad (29)$$

where $D_y : \{|y| < g_0\}$ and $D_\theta : \{|\theta| < \theta_{\max} = \tan^{-1}\frac{g_0}{L}\}$.

In order to solve such nonlinear optimization problem with the strict constrained conditions of y and θ, the nonlinear Interior Point (IP) or Sequential Quadratic Programming (SQP) methods are utilized [17]. The numerical result of $V_{y,\theta-cr}$ is compared to the analytical solutions of $V_{\theta-cr}$ and V_{y-cr} obtained from Equations (17) and (21), respectively, in Figure 6. Obviously, the critical voltage considering both the translational and rotational displacements is always less than those considering one of them. For the folded beam suspension mechanism studied in this paper, V_{y-cr} dramatically drops while $V_{\theta-cr}$ only slightly (and linearly) decreases when x approaches its maximum $X_{\max}$. In this case, the effect of lateral translation should be more concerned since V_{y-cr} is much closer to $V_{y,\theta-cr}$ than $V_{\theta-cr}$ at the extreme position of the proof mass.
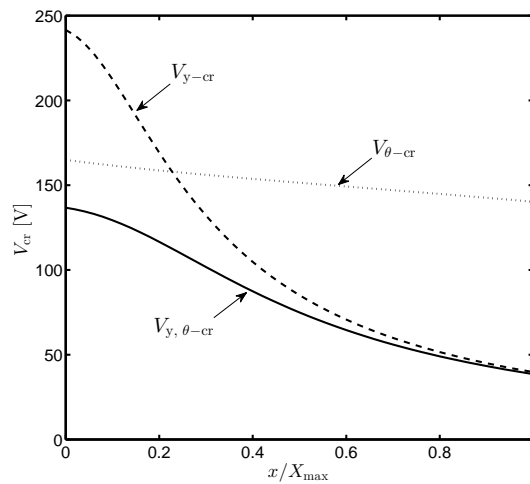

Figure 6. Comparison of the critical voltages in three analyzed cases: rotational instability $V_{\theta-cr}$ or translational instability V_{y-cr}, alone or in combination $V_{y,\theta-cr}$.

2.6. Critical Voltage with Translational and Rotational Offsets

Typically, for the overlap-varying electrostatic transducers, the movable fingers are placed in between the fixed ones. However, there is a possibility that translational and rotational offsets exist, i.e., y_0 and θ_0, respectively, due to manufacturing tolerance or error in the fabrication process. This unexpectedly can lead to further reduction of the critical voltage. The value of $V_{y,\theta-cr}$ at $x = X_{\max}$ is investigated since it is the maximum voltage that can be applied between the two electrodes while still ensuring the transducer stability.

When $x = X_{\max} \approx x_0 \approx L/2$, the moment and force equilibrium conditions in Equation (24) become

$$
\begin{bmatrix} -K_y + \frac{1}{2}V^2 A & \frac{1}{2}V^2 B \\ \frac{1}{2}V^2 C & -K_\theta + \frac{1}{2}V^2 D \end{bmatrix} \begin{bmatrix} y_0 + \Delta y \\ \theta_0 + \Delta \theta \end{bmatrix} = \begin{bmatrix} 0 \\ 0 \end{bmatrix},
\tag{30}
$$

where

$$
A = \frac{2C_0 g_0^2 L}{x_0 \left(g_0 + L(\theta_0 + \Delta\theta)\right)^2 \left(g_0 - L(\theta_0 + \Delta\theta)\right)^2},
\tag{31}
$$

$$
B = \frac{C_0 g_0^2 L^2 \left(g_0^2 + 3(y_0 + \Delta y)^2\right)}{\left(g_0 - (y_0 + \Delta y)\right)^3 \left(g_0 + (y_0 + \Delta y)\right)^3},
\tag{32}
$$

$$
C = \frac{C_0 L^2 \left(g_0^2 + L^2(\theta_0 + \Delta\theta)^2\right)}{x_0 \left(g_0 - L(\theta_0 + \Delta\theta)\right)^2 \left(g_0 + L(\theta_0 + \Delta\theta)\right)^2},
\tag{33}
$$

$$
D = \frac{2}{3} \frac{C_0 g_0^2 \left(g_0^2 + 3(y_0 + \Delta y)^2\right) L^3}{x_0 \left(g_0 - (y_0 + \Delta y)\right)^3 \left(g_0 + (y_0 + \Delta y)\right)^3}.
\tag{34}
$$

The critical voltage is the intersection of two surfaces determined by

$$
\begin{cases} V = \sqrt{\dfrac{2K_y(y_0 + \Delta y)}{A(y_0 + \Delta y) + B(\theta_0 + \Delta\theta)}}, \\[3mm] V = \sqrt{\dfrac{2K_\theta(\theta_0 + \Delta\theta)}{C(y_0 + \Delta y) + D(\theta_0 + \Delta\theta)}}. \end{cases}
\tag{35}
$$

Figure 7 presents the 3D curve of the critical voltage determined by the intersection of two surfaces on the right-hand side of the equation system (35).
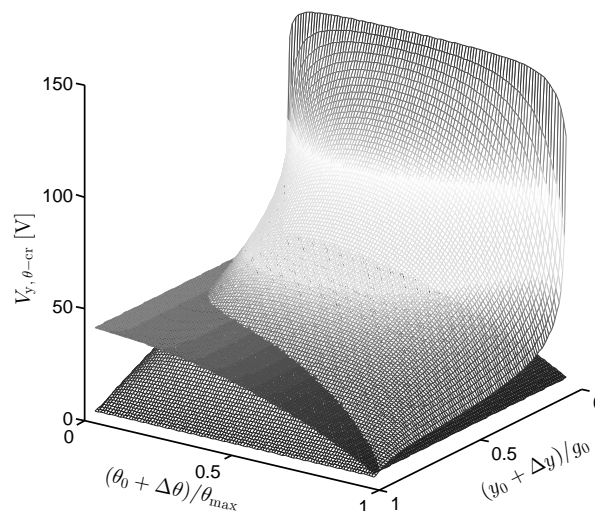

Figure 7. The intersection of two surfaces versus variation of the translational and rotational displacement, which determines the critical voltage.

The critical voltage is now expressed as

$$
V^*_{y,\theta-cr} = \max \left\{ V \in \overline{V}^* \right\},
\tag{36}
$$

where $\overline{V}^*$ is a set of V such that Equation (30) has solutions $\Delta y \in D^*_{\Delta y}$ and $\Delta\theta \in D^*_{\Delta\theta}$, with $D^*_{\Delta y} : \{-g_0 - y_0 < \Delta y < g_0 - y_0\}$ and $D^*_{\Delta\theta} : \{-\theta_{\max} - \theta_0 < \Delta\theta < \theta_{\max} - \theta_0, \ \theta_{\max} = \tan^{-1}\frac{g_0}{L}\}$. As aforementioned, $V^*_{y,\theta-cr}$ can be solved numerically by utilizing the nonlinear constrained

optimization methods such as IP or SQP. To exhibit the effect of offsets on the critical voltage, there are two special cases where $(\theta_0 = 0, y_0 \neq 0)$ or $(\theta_0 \neq 0, y_0 = 0)$ are separately considered.

Figure 8 depicts numerical solutions of the critical voltage when the translational and rotational offsets are taken into account. In a general trend, the larger the lateral off-sets, the bigger the critical voltage reduction. When $\theta_0 = 0$, the critical voltage $V^*_{y,\theta-cr}$ is almost unchanged if the ratio $y_0/g_0 \leq 0.6$ and dramatically reduces with further increase of y_0/g_0. In case of $y_0 = 0$, $V^*_{y,\theta-cr}$ gradually decreases with rise of θ_0/θ_{max}.
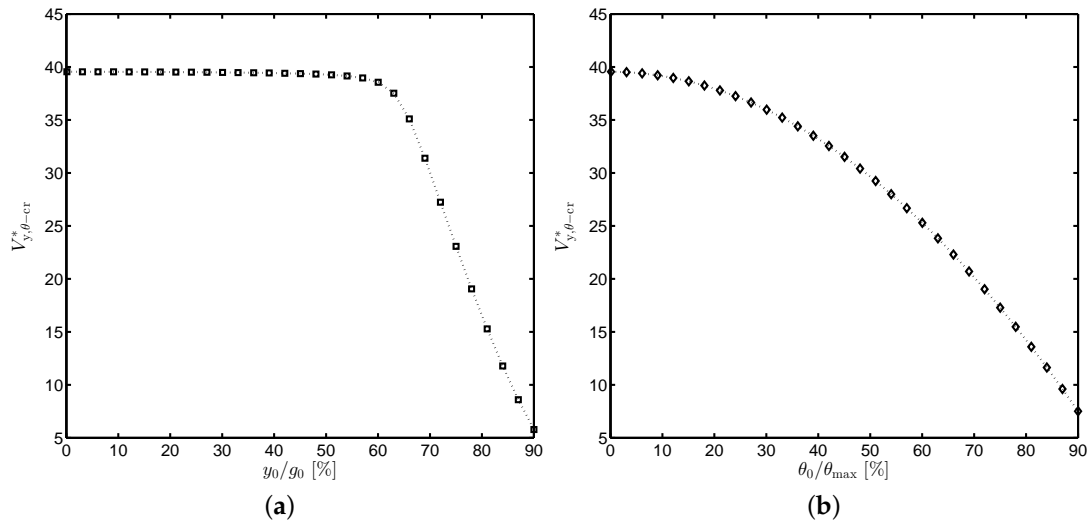

Figure 8. The reduction of the critical voltage taking into account the effects of misalignment offsets. (**a**) $V^*_{y,\theta-cr}$ $(y_0 \neq 0, \theta_0 = 0)$, (**b**) $V^*_{y,\theta-cr}$ $(y_0 = 0, \theta_0 \neq 0)$.

3. Analysis of a Comb-Drive Harvesters with Two Anti-Phase Capacitors

3.1. Differential Common Modes

For the versatility, the overlap-varying anti-phase transducers are used in many applications, such as sensing and actuating [5,18–20]. Considering common configurations of such structure represented in Figure 9, the electrostatic energy is

$$W_e = -\frac{1}{2}(C_A + C_B)V^2, \tag{37}$$

where $C_A = C_1 + C_2$ and $C_B = C_3 + C_4$. C_1 and C_2 are referred to (4) and (5), while C_3 and C_4 are calculated as

$$C_3(x, y, \theta) = C_0 \frac{g_0}{2x_0 \sin \theta} \ln \frac{g_0 + y + L \sin \theta}{g_0 + y + (L - (x_0 - x)) \sin \theta}, \tag{38}$$

$$C_4(x, y, \theta) = C_0 \frac{g_0}{2x_0 \sin \theta} \ln \frac{g_0 - y - (L - (x_0 - x)) \sin \theta}{g_0 - y - L \sin \theta}. \tag{39}$$

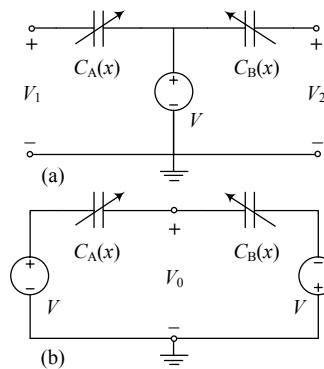The coefficients of the stiffness matrix in (24) can be found in Appendix A.

Figure 9. Circuit diagram for two common configurations of overlap-varying anti-phase transducers.

3.2. Bennet's Doubler Configuration

We are now widening the problem of lateral instability for a more general circumstance where the voltages V_a and V_b across C_A and C_B respectively are not equal. To be specific, the overlap-varying transducers configured as Bennet's doubler represented in Figure 10 is investigated. An analytical solution (utilizing mathematically-idealized diode model) developed in [21] shows that: V_a and V_b can be captured by Direct Current (DC) offset sinusoidal signals when the doubler circuit reaches saturation. For the static pull-in instability analysis, the DC offset voltages on C_A and C_B are considered and respectively expressed as

$$V_A = V_s \frac{1 + \sqrt{5}}{4}, \tag{40}$$

$$V_B = V_s \frac{3 + \sqrt{5}}{4}, \tag{41}$$

where V_s is the saturation DC voltage at output. The electrostatic energy is

$$W_e = -\frac{1}{2} V_s^2 \left(\frac{3 + \sqrt{5}}{8} C_A + \frac{7 + 3\sqrt{5}}{8} C_B \right). \tag{42}$$

Similarly, the complete global stiffness matrix can be obtained by taking the derivative of the moment and forces, see Appendix B for more details.
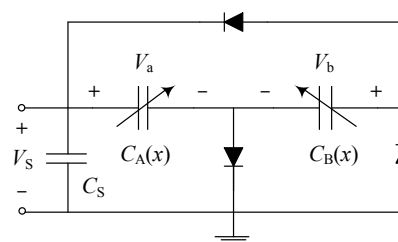

Figure 10. Bennet's doubler configuration of the overlap-varying anti-phase transducers.

3.3. Numerical Results

Using the same optimization procedure as presented in previous sections, the critical voltage is numerically obtained in Figure 11. For the common configurations shown in Figure 9, there is a significant reduction of $V_{y,\theta-cr}$, i.e., more than 10 V, compared to the case in which the single-capacitance transducer is investigated. $V_{y,\theta-cr}$ of the doubler circuit also decreases with the increase of the proof mass displacement but is less sensitive than the two former circumstances.
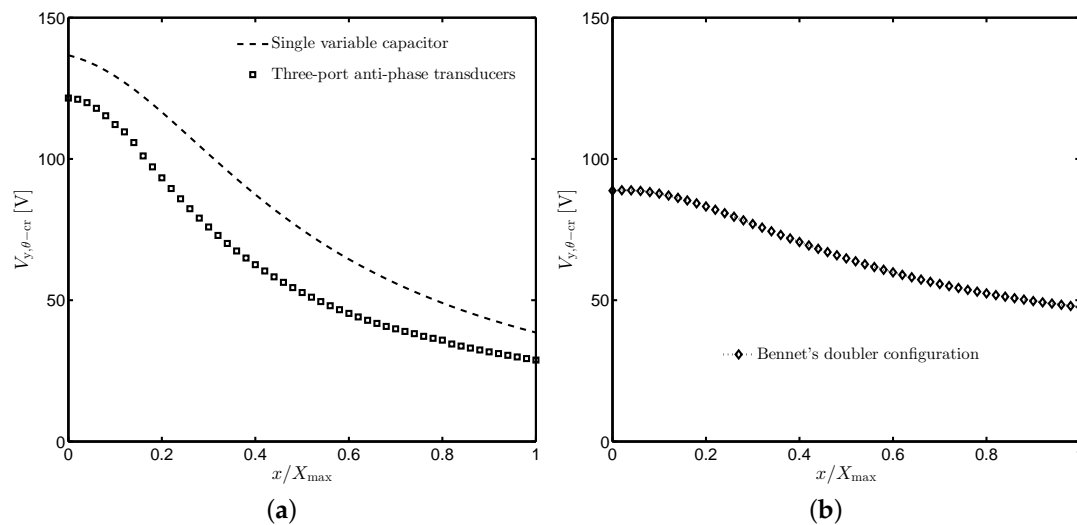
Figure 11. Comparison of the critical voltages for the single-capacitance transducer and different configurations of the one with anti-phase capacitors. (**a**) Anti-phase operation mode, (**b**) Bennet's doubler configuration.

4. Discussion

In principle, the pull-in phenomenon is the loss of the equilibrium stability, from which one should distinguish the difference between the static and dynamic pull-in aspects. The static conditions based on potential energy are for local stability; they are only applicable for small displacement near the equilibrium point. Younis [22] presented a universal definition of dynamic pull-in, which is the collapse of the movable electrode into the stationary one due to the combined action of the kinetic and potential energies. For the considered transducers, a source of kinetic energy is from the Alternating Current (AC) harmonic voltages. The dynamic pull-in generally occurs at lower DC voltage compared to that of static pull-in, see [23] for an example. Dynamic pull-in instability, therefore, can be considered as a key source of failure in MEMS electrostatic devices. It is more of interest for sophisticated configurations that have been studied and is an open issue for further investigations.

When the overlap-varying transducers are configured as Bennet's doubler, the max/min ratio of capacitance variation needs to be larger than 2 to allow operation of the circuit [24]. The travel range of the proof mass is now more important, which is fundamentally dictated by inherent pull-in instability. In attempts to enlarge the stable displacement for MEMS electrostatic devices, several improvements of the suspension beam designs have been developed. Zhou et al. proposed a tilted folded-beam suspension to shift the maximum of the lateral spring constant curve and thus prevent the pull-in limited travel range of the comb-drives [11]. For more recent work, Olfatnia et al. presented a novel clamped paired double parallelogram flexure mechanism. This structure offers high stroke direction stiffness K_x while maintaining low translational and rotational stiffnesses K_y and K_θ over a large range of proof mass displacement [16]. These advanced methods can be extremely useful to overcome the challenges in enhancing the stable range.

5. Conclusions

This paper presents a further development of a 2D model utilization to analyze the lateral pull-in instability of an in-plane overlap-varying transducer. Analytical solutions of the critical voltage are derived when the translational and rotational displacements are separately considered. The ratio of rotational and translational critical voltages in these two cases can be made large by appropriate choice of the dimensions D_1 and D_2 of the folded-beam spring. The numerical result for the general case is determined, taking into account the combination of both lateral translation and rotation. The effects of

translational and rotational offsets to the critical voltage are explored numerically. All analysis results are adaptable and applicable to different types of the mechanical spring, and therefore can be used as a guideline for MEMS transducer design.

Appendix A. Anti-Phase Operation Mode

With $\sin\theta \approx \theta$, the coefficients of the stiffness matrix in (24) would take the forms

$$
\begin{aligned}
\frac{\partial F_y}{\partial y}\bigg|_{y\to 0} = -K_y + \frac{1}{4}V^2\frac{C_0 g_0}{x_0}\bigg[& \frac{x_0+x}{(g_0+L\theta)\left(g_0+(L-(x_0+x))\theta\right)^2} + \frac{x_0+x}{(g_0+L\theta)^2\left(g_0+(L-(x_0+x))\theta\right)} \\
& + \frac{x_0+x}{(g_0-L\theta)\left(g_0-(L-(x_0+x))\theta\right)^2} + \frac{x_0+x}{(g_0-L\theta)^2\left(g_0-(L-(x_0+x))\theta\right)} \\
& + \frac{x_0-x}{(g_0+L\theta)\left(g_0+(L-(x_0-x))\theta\right)^2} + \frac{x_0-x}{(g_0+L\theta)^2\left(g_0+(L-(x_0-x))\theta\right)} \\
& + \frac{x_0-x}{(g_0-L\theta)\left(g_0-(L-(x_0-x))\theta\right)^2} + \frac{x_0-x}{(g_0-L\theta)^2\left(g_0-(L-(x_0-x))\theta\right)}\bigg],
\end{aligned}
\tag{A1}
$$

$$
\frac{\partial F_y}{\partial \theta}\bigg|_{\theta\to 0} = -V^2\frac{C_0 g_0^2}{x_0}\frac{\left(g_0^2+3y^2\right)\left(x_0^2+x^2-2Lx_0\right)}{(g_0-y)^3(g_0+y)^3},
\tag{A2}
$$

$$
\begin{aligned}
\frac{\partial M_\theta}{\partial y}\bigg|_{y\to 0} = \frac{1}{4}V^2\frac{C_0 g_0}{\theta x_0}\bigg[& -\frac{x_0+x}{(g_0-L\theta)\left(g_0-(L-(x_0+x))\theta\right)} - \frac{x_0-x}{(g_0-L\theta)\left(g_0-(L-(x_0-x))\theta\right)} \\
& + \frac{x_0-x}{(g_0+L\theta)\left(g_0+(L-(x_0-x))\theta\right)} + \frac{x_0+x}{(g_0+L\theta)\left(g_0+(L-(x_0+x))\theta\right)} \\
& + \frac{(x_0+x)g_0}{(g_0-L\theta)^2\left(g_0-(L-(x_0-x))\theta\right)} + \frac{(x_0-x)g_0}{(g_0-L\theta)^2\left(g_0-(L-(x_0-x))\theta\right)} \\
& + \frac{L\theta(x_0-x)}{(g_0+L\theta)^2\left(g_0+(L-(x_0-x))\theta\right)} + \frac{L\theta(x_0+x)}{(g_0+L\theta)^2\left(g_0+(L-(x_0+x))\theta\right)} \\
& + \frac{\theta(x_0+x)\left(L-(x+x_0)\right)}{(g_0-L\theta)\left(g_0-(L-(x_0+x))\theta\right)^2} + \frac{\theta(x_0-x)\left(L-(x_0-x)\right)}{(g_0-L\theta)\left(g_0-(L-(x_0-x))\theta\right)^2} \\
& - \frac{g_0(x_0-x)}{(g_0+L\theta)\left(g_0+(L-(x_0-x))\theta\right)^2} - \frac{g_0(x_0+x)}{(g_0+L\theta)\left(g_0+(L-(x_0+x))\theta\right)^2}\bigg],
\end{aligned}
\tag{A3}
$$

$$
\frac{\partial M_\theta}{\partial \theta}\bigg|_{\theta\to 0} = -K_\theta + \frac{2}{3}V^2\frac{C_0 g_0^2}{x_0}\frac{\left(g_0^2+3y^2\right)\left(3L^2 x_0 - 3L^2 x^2 - 3Lx_0^2 + 3x^2 x_0 + x_0^3\right)}{(g_0-y)^3(g_0+y)^3}.
\tag{A4}
$$

Appendix B. Bennet's Doubler Configuration

For the doubler configuration, the coefficients of the stiffness matrix in (24) are

$$\left.\frac{\partial F_y}{\partial y}\right|_{y\to 0} = -K_y + V^2\frac{C_0 g_0^2}{x_0\left(g_0^2 - L^2\theta^2\right)^2}$$

$$\left[\frac{p(x_0-x)\left(g_0^4 + 2g_0^2 L\theta^2(L-(x_0-x)) - L\theta^4\left(3L^3 - 6L^2(x_0-x) + 4L(x_0-x)^2 - (x_0-x)^3\right)\right)}{\left(g_0^2 - \theta^2\left(L-(x_0-x)\right)^2\right)^2}\right.$$

$$\left.+\frac{q(x_0+x)\left(g_0^4 + 2g_0^2 L\theta^2(L-(x_0+x)) + L\theta^4\left(-3L^3 + 6L^2(x_0+x) - 4L(x_0+x)^2 + (x_0+x)^3\right)\right)}{\left(g_0^2 - \theta^2\left(L-(x+x_0)\right)^2\right)^2}\right], \tag{A5}$$

$$\left.\frac{\partial F_y}{\partial\theta}\right|_{\theta\to 0} = -\frac{1}{2}V^2\frac{C_0 g_0^2\left(g_0^2 + 3y^2\right)\left(-2L(p(x_0-x)+q(x_0+x))+p(x_0-x)^2+q(x_0+x)^2\right)}{x_0\left(g_0^2 - y^2\right)^3}, \tag{A6}$$

$$\left.\frac{\partial M_\theta}{\partial y}\right|_{y\to 0} = \frac{1}{2}V^2\frac{C_0 g_0^2}{x_0}\left[\frac{2p(x_0-x)(2L-(x_0-x))\left(g_0^4 - L^2\theta^4\left(L-(x_0-x)\right)^2\right)}{\left(g_0^2 - L^2\theta^2\right)^2\left(g_0^2 - \theta^2\left(L-(x_0-x)\right)^2\right)^2}\right.$$

$$+\frac{2q(x_0+x)(2L-(x_0+x))\left(g_0^4 - L^2\theta^4\left(L-(x_0+x)\right)^2\right)}{\left(g_0^2 - L^2\theta^2\right)^2\left(g_0^2 - \theta^2\left(L-(x_0+x)\right)^2\right)^2} \tag{A7}$$

$$\left.-\frac{p(x_0-x)(2L-(x_0-x))}{\left(g_0^2 - L^2\theta^2\right)\left(g_0^2 - \theta^2\left(L-(x_0-x)\right)^2\right)} - \frac{q(x_0+x)(2L-(x_0+x))}{\left(g_0^2 - L^2\theta^2\right)\left(g_0^2 - \theta^2\left(L-(x_0+x)\right)^2\right)}\right],$$

$$\left.\frac{\partial M_\theta}{\partial\theta}\right|_{\theta\to 0} = -K_\theta + \frac{1}{3}V^2\frac{C_0 g_0^2\left(g_0^2 + 3y^2\right)}{x_0\left(g_0^2 - y^2\right)^3}\left[3L^2(p(x_0-x)+q(x_0+x))\right.$$

$$\left.-3L\left(p(x_0-x)^2 + q(x_0+x)^2\right) + p(x_0-x)^3 + q(x_0+x)^3\right], \tag{A8}$$

where

$$p = \frac{1+\sqrt{5}}{4}, \tag{A9}$$

$$q = \frac{3+\sqrt{5}}{4}. \tag{A10}$$

References

1. Meninger, S.; Mur-Miranda, J.; Amirtharajah, R.; Chandrakasan, A.; Lang, J. Vibration-to-electric energy conversion. *IEEE Trans. Very Large Scale Integr. (VLSI) Syst.* **2001**, *9*, 64–76. [CrossRef]
2. Roundy, S.; Pister, K.S.J.; Wright, P.K. Micro-electrostatic vibration-to-electricity converters. In Proceedings of the IMECE2002, ASME International Mechanical Engineering Congress & Exposition, New Orleans, LA, USA, 17–22 November 2002.
3. Tang, W.C.; Nguyen, T.-C.H.; Judy, M.W.; Howe, R.T. Electrostatic-comb drive of lateral polysilicon resonators. *Sens. Actuators A Phys.* **1990**, *21*, 328–331. [CrossRef]
4. Adams, S.G.; Bertsch, F.M.; Shaw, K.A.; Hartwell, P.G.; Moon, F.C.; MacDonald, N.C. Capacitance based tunable resonators. *J. Micromech. Microeng.* **1998**, *8*, 15. [CrossRef]
5. Hirano, T.; Furuhata, T.; Gabriel, K.J.; Fujita, H. Design, fabrication, and operation of submicron gap comb-drive microactuators. *J. Microelectromech. Syst.* **1992**, *1*, 52–59. [CrossRef]

6.   Jaecklin, V.P.; Linder, C.; de Rooij, N.F.; Moret, J.M. Micromechanical comb actuators with low driving voltage. *J. Micromech. Microeng.* **1992**, *2*, 250. [CrossRef]

7.   Truong, B.D.; Le, C.P.; Halvorsen, E. Analysis of electrostatic energy harvesters electrically configured as Bennet's doublers. *IEEE Sens. J.* **2017**, *17*, 5180–5191. [CrossRef]

8.   Truong, B.D.; Le, C.P.; Halvorsen, E. Analysis of MEMS electrostatic energy harvesters electrically configured as voltage multipliers. *AEU Int. J. Electron. Commun.* **2019**, *107*, 125–136. [CrossRef]

9.   Nathanson, H.C.; Newell, W.E.; Wickstrom, R.A.; Davis, J.R. The resonant gate transistor. *IEEE Trans. Electr. Devices* **1967**, *14*, 117–133. [CrossRef]

10.   Legtenberg, R.; Groeneveld, A.W.; Elwenspoek, M. Comb-drive actuators for large displacements. *J. Micromech. Microeng.* **1996**, *6*, 320. [CrossRef]

11.   Zhou, G.; Dowd, P. Tilted folded-beam suspension for extending the stable travel range of comb-drive actuators. *J. Micromech. Microeng.* **2003**, *13*, 178. [CrossRef]

12.   Avdeev, I.V.; Lovell, M.R.; Onipede, O., Jr. Modeling in-plane misalignments in lateral combdrive transducers. *J. Micromech. Microeng.* **2003**, *13*, 809. [CrossRef]

13.   Huang, W.; Lu, G. Analysis of lateral instability of in-plane comb drive MEMS actuators based on a two-dimensional model. *Sens. Actuators A Phys.* **2004**, *113*, 78–85. [CrossRef]

14.   Grade, J.D.; Jerman, H.; Kenny, T.W. Design of large deflection electrostatic actuators. *J. Microelectromech. Syst.* **2003**, *12*, 335–343. [CrossRef]

15.   Chen, C.; Lee, C. Design and modeling for comb drive actuator with enlarged static displacement. *Sens. Actuators A Phys.* **2004**, *115*, 530–539. [CrossRef]

16.   Olfatnia, M.; Sood, S.; Gorman, J.J.; Awtar, S. Large stroke electrostatic comb-drive actuators enabled by a novel flexure mechanism. *J. Microelectromech. Syst.* **2013**, *22*, 483–494. [CrossRef]

17.   Jorge Nocedal, S.W. *Numerical Optimization*, 2nd ed.; Springer Series in Operations Research; Springer: New York, NY, USA, 2006.

18.   Yu, Y.; Yuan, W.; Sun, R.; Qiao, D.; Yan, B. A strategy to efficiently extend the change rate of period for comb-drive micromechanical pitch-tunable gratings. *J. Microelectromech. Syst.* **2010**, *19*, 1180–1185. [CrossRef]

19.   Chang, C.-M.; Wang, S.-Y.; Chen, R.; Yeh, J.A.; Hou, M.T. A comb-drive actuator driven by capacitively-coupled-power. *Sensors* **2012**, *12*, 10881–10889. [CrossRef] [PubMed]

20.   Hou, M.T.; Huang, M.-X.; Chang, C.-M. Nested folded-beam suspensions with low longitudinal stiffness for comb-drive actuators. *J. Micromech. Microeng.* **2014**, *24*, 125022. [CrossRef]

21.   Truong, B.D.; Le, C.P.; Halvorsen, E. Theoretical analysis of electrostatic energy harvester configured as Bennet's doubler based on Q-V cycles. *arXiv* **2017**, arXiv:1709.08754.

22.   Younis, M.I. *Introduction to Nonlinear Dynamics*; Springer: Boston, MA, USA, 2011; pp. 155–249.

23.   Elata, D.; Bamberger, H. On the dynamic pull-in of electrostatic actuators with multiple degrees of freedom and multiple voltage sources. *J. Microelectromech. Syst.* **2006**, *15*, 131–140. [CrossRef]

24.   De Queiroz, A.C.M.; Domingues, M. Electrostatic energy harvesting using doublers of electricity. In Proceedings of the 2011 IEEE 54th International Midwest Symposium on Circuits and Systems (MWSCAS), Seoul, Korea, 7–10 August 2011; pp. 1–4.